Article

Not peer-reviewed version

New Insights into Renal Neoplasm Differentiation: Nonlinear Microscopy's Breakthrough Advantages

Gorana Nikolic [†] , Maja Zivotic [†] , Ana Mioljevic , Sanja Despotovic , Stanko Nenad Nikolic ,
Mihailo Rabasovic , Sanja Radojevic Skodric , Lidija Matija [*]

Posted Date: 30 October 2023

doi: 10.20944/preprints202310.1864.v1

Keywords: Multiphoton microscopy; nonlinear microscopy; renal cell tumors; tumor capsule; twophoton excitation fluorescence; three-photon fluorescence; second harmonic generation

Article

New Insights into Renal Neoplasm Differentiation: Nonlinear Microscopy's Breakthrough Advantages

Gorana Nikolic [1,2,*,†], Maja Zivotic [1,2,†], Ana Mioljevic [2], Sanja Despotovic [2,3], Stanko Nikolic [4], Mihailo Rabasovic [4], Sanja Radojevic Skodric [1,2] and Lidija Matija [5,*]

[1] Institute for Pathology, Faculty of Medicine University of Belgrade, Serbia
[2] Faculty of Medicine University of Belgrade, Serbia
[3] Institute for Histology and Embryology "Aleksandar Đ. Kostić" Faculty of Medicine, University of Belgrade
[4] Institute of Physics Belgrade, University of Belgrade, Serbia
[5] Department of Biomedical Engineering, Faculty of Mechanical Engineering, University of Belgrade, Serbia
[*] Correspondence: GN gorana.nikolic@med.bg.ac.rs, gorana.nikolic03@gmail.com; LM lmatija@mas.bg.ac.rs
[†] These authors contributed equally to this work.

Abstract: Multiphoton microscopy (MPM) is a cutting-edge nonlinear microscopy technique known for its exceptional capabilities in imaging dense tissues, making it an ideal tool for exploring human kidney tissue. This study delves into the application of MPM in evaluating renal cell tumors and characterizing tumor capsules. MPM encompasses two core methods: two-photon excitation fluorescence (TPEF) and second harmonic generation (SHG). It leverages femtosecond lasers to provide deep tissue imaging while minimizing phototoxicity, making it well-suited for live tissue analysis. The study analyzed 100 formalin-fixed paraffin-embedded (FFPE) kidney tissue samples, ensuring compliance with ethical standards. Using a Ti:Sapphire laser for femtosecond pulses and a variety of optical components and filters, the researchers captured TPEF and SHG signals, facilitating image analysis. Normal kidney tissue exhibited distinctive structures like glomeruli and tubules under MPM. Renal cell carcinoma (ccRCC) displayed unique TPEF patterns with eccentrically located nuclei and indistinct cytoplasmic membranes. Papillary RCC (pRCC) exhibited a papillary pattern with dark nuclei, while chromophobe RCC (chRCC) showcased distinct features like thick cell membranes, strong TPEF signal in nuclei, and granular cytoplasm. Renal oncocytoma (RO) presented strong TPEF signals in cuboidal cells with microcyst-like arrangements. Overall, MPM proved invaluable in assessing human kidney tissue, offering distinct TPEF patterns for different renal cell tumor types. This non-invasive technique has the potential to enhance pathological examinations and advance our understanding of complex biological processes, ultimately contributing to improved diagnostics and treatment strategies for renal diseases.

Keywords: Multiphoton microscopy; nonlinear microscopy; renal cell tumors; tumor capsule; two-photon excitation fluorescence; three-photon fluorescence; second harmonic generation

---

1. Introduction

Multi-photon microscopy (MPM) represents a non-linear microscopy (NLM) technique that has emerged as the gold standard for fluorescence microscopy in dense tissue and thick sections (1). MPM combines two distinct methods. The first method considers two-photon excitation fluorescence (TPEF), enabling the observation of autofluorescence (AF) in unstained living tissue by detecting intrinsic emissions from molecules like nicotinamide adenine dinucleotide (NADH) and flavin adenine dinucleotide (FAD) within cells (2,3). The second MPM method incorporates second harmonic generation (SHG), as a process that facilitates the visualization of non-centrosymmetric structures such as collagen fibers through scattering effects (4). By utilizing chemical clearing techniques in conjunction with MPM, it becomes possible to achieve tissue penetration depths of up to 1 cm (5).

Nonlinear optical phenomena in nanomaterials (NMs) can be categorized into two main types: non-parametric and parametric processes, as described by Mertz in 2004(6). Non-parametric processes involve changes between the initial and final quantum states of active molecules. One prominent example is multiphoton fluorescence. Specifically, two-photon fluorescence (2PF) plays a significant role in NM studies, especially when used in conjunction with common biological fluorophores like fluorescent proteins, intracellular probes, and ion indicators (6,7).

An essential benefit offered by nanomaterials (NMs) is their ability to facilitate deep tissue imaging, surpassing the constraints imposed by light scattering in conventional linear microscopy, especially within the visible wavelength range (8). In recent applications, a technique known as three-photon fluorescence (3PF) has gained prominence. This method significantly improves signal-to-background ratios compared to two-photon fluorescence (2PF) and opens up possibilities for exceptionally deep imaging (9) . For instance, researchers have successfully employed 3PF for in vivo imaging, allowing them to visualize labeled neurons located at depths ranging from 500 to 1100 μm within intact mouse brains (10,11).

A significant progress in the microscopic imaging of various types of cells and tissues in the biological and medical sciences was enabled by the use of the femtosecond lasers. These devices emit coherent light radiation in the form of a train of extremely short electromagnetic pulses whose duration lies in the range from a few to several hundred femtoseconds (1 fs = 10-15 s).

Although the energy per pulse usually equals several tens of nanojoules, its optical power may reach values of the order of megawatts. If the laser beam is focused on the sample, the intensity per pulse becomes very high, which leads to the appearance of multiphoton absorption or other nonlinear effects in the focal volume (12,13). The result of these interactions is the fluorescent radiation that provides information about the sample that emits it. On the basis of these physical effects, a number of new microscopic methods have been developed, known as MPM techniques. They are characterized by the sophisticated methods of excitation and detection of fluorescence from the sample, which significantly improves the microscopic resolution and the possibility for three-dimensional (3D) imaging, compared to classical optical microscopy (14,15). The advantages of MPM techniques are reduced photobleaching, phototoxicity and photodamage of the specimen (compared to confocal microscopy), because the corresponding nonlinear interactions occur only in the focal volume where the intensity of the laser beam is high enough. Additionally, the use of excitation infrared laser radiation leads to deeper penetration of light into tissue due to less scattering and reduced absorption in cellular proteins (8). Nowadays, the commonly used standard method in pathology is staining with haematoxylin and eosine (H&E). However, this rather simple method is limited to ex vivo investigations, whereas the MPM techniques are therefore an excellent choice for imaging living and intact biological tissues at wavelengths ranging from the molecular level to the dimensions of the entire sample (16-18). MPM is particularly convenient for performing minimally invasive experimental measurements over long periods of time. It may provide exquisite details of inherently dynamic biological processes that take place on timescales from microseconds to even days or weeks. As a result, large amounts of data are available to further improve the understanding of complex biological interactions (19).

Over the past two decades, MPM has been widely used for detection and evaluation of numerous different tumors, benign and malignant, in various conditions, as well as identifying the presence of tumor capsule (20).

Considering all the advantages of MPM techniques, we intended to widely explore its application in the assessment of human kidney tissue, emphasizing the advantages of its usage in detection and differentiation of renal cell tumors including the presence and characteristics of tumor capsule.

2. Materials and Methods

The research work presented in this paper was conducted using a NLM experiment developed in the Laboratory for Biophysics at the Institute of Physics Belgrade. The microscopic image is obtained by measuring the TPEF or SHG signal. The 96 analyzed samples were formalin-fixed paraffin-embedded (FFPE) blocks tissues of kidney tumors as well as healthy tissue collected from the Department of Urologic Pathology, University Clinical Center of Serbia, Belgrade. The study was conducted following all ethical standards laid down in the 1964 Declaration of Helsinki. The study was carried out retrospectively, according to our ethical guidelines, therefore informed consent of patients was not required, however, the Ethics Committee of the Clinic of Urology of Clinical Center of Serbia approved collecting the samples from the archive and carrying out the study (Application Ref: 0152/20, dated March 4th, 2020).

Experimental setup

A Ti:Sapphire laser (Coherent, Mira 900-F) was used to generate a train of femtosecond pulses with a wavelength in the range from 700 to 1000 nm, pulse duration of 160 fs and a 76 MHz repetition frequency. A Yb:KGW femtosecond laser (Time-Bandwidth Products AG, Yb GLX) with an emission wavelength of 1040 nm was also used. A variable optical density filter was placed in front of the laser aperture and used to adjust the optical power. The lens system expands the diameter of the laser beam, which is then directed onto the dichroic mirror. A dichroic mirror (Thorlabs, M254H45) is used for two purposes: to reflect the laser beam to the objective and to transmit the TPEF and SHG signals to the photomultiplier tube (PMT) (RCA, PF1006).

Two mirrors on galvanometers (Cambridge Technologies, 6215H) were used for raster scanning of the beam on a sample. In this way, the signal is collected from different points in a specimen plane and a two-dimensional image is generated. For the analysis of NLM measurements, one 10 μm section was cut from all the samples. The samples were then deparaffinized and hydrated, afterwards covered with glycer gel and placed in a refrigerator. The laser beam is focused on the sample using an objective (Carl Zeiss, EC Plan-NEOFLUAR, 40× / 1.3 oil). A camera (Canon EOS 50D) is used to capture the sample in the bright field. To perform system alignment, we removed the infrared blocking filter from our commercial camera to view the backscatter/back reflection of the laser spot from the sample/coverslip. This is possible since a small fraction of the laser light is transmitted through the dichroic mirror. Then, a mirror or beam splitter is used to reflect a part or overall signal onto the PMT. A filter is placed in front of the PMT to transmit the useful signal and remove the scattered laser light. During the detection of the TPEF signal, different broadband filters (around 40 nm) were used, transparent in the visible light region, while the wavelengths in the IR and UV regions were blocked. For the SHG signal detection, a narrow-band filter, transparent only for a wavelength twice shorter than the laser beam wavelength (± 5 nm), was used.

The excitation wavelength was chosen so that the fluorescent signal originates predominantly from the renal structures of interest. Therefore, a broadband filter was used for the TPEF measurements, which ensures that all fluorescent light is collected, even from the wings of the fluorescent spectrum. This is important in the case of relatively low excitation efficiency and ensures a good signal-to-noise ratio and high image contrast. The TPEF image was captured using laser emission with a wavelength in the range of 730 - 980 nm and an optical power of 8.2 to 20 mW in the plane of the sample. This power range was chosen to minimize photodamage of the kidney tissue samples. Different combinations of laser excitation wavelengths and filters were tested to preferentially excite NADH or FAD and obtain the sharpest image. In the measurements, excitation at 730 nm and the use of VIS filters (from 415 to 685 nm) were most frequently used due to the best image quality (maximal signal-to-noise ratio).

All FFPE were cut into 10 μm thick sections, deparaffinized and rehydrated, and after that covered with coverslip using glycer gel without any staining.

3. Results

The study included 96 patients diagnosed with the most frequent pathohistological types of renal cell tumours, such as clear cell renal cell carcinoma (ccRCC), papillary renal cell carcinoma (pRCC), chromophobe renal cell carcinoma (chRCC) and renal oncocytoma (RO). We evaluated 43 samples diagnosed as ccRCC, 15 pRCC cases, 20 cases of chRCC, and 18 cases diagnosed as RO. Based on hematoxylin and eosin (H&E), histochemical (HC), and immunohistochemical (IHC) slides, diagnoses were reviewed by two experienced uropathologists using light microscopy (LM). Furthermore, we analyzed healthy kidney tissue as well.

The structures of a normal kidney tissue, i.e., glomerulus, proximal and distal tubules and interstitium were observed using an optical microscope (Figure 1A). The same structures can be seen on NLM on non-stained tissue slides (Figure 1B). In the center of the NLM picture, the glomerulus is seen surrounded by both proximal and distal tubules. Epithelial cells of the tubules are cuboidal-shaped and the nucleus has a lower TPEF signal, presented as a dark area. The autofluorescence presented as a is in the glomerulus is erythrocytes.

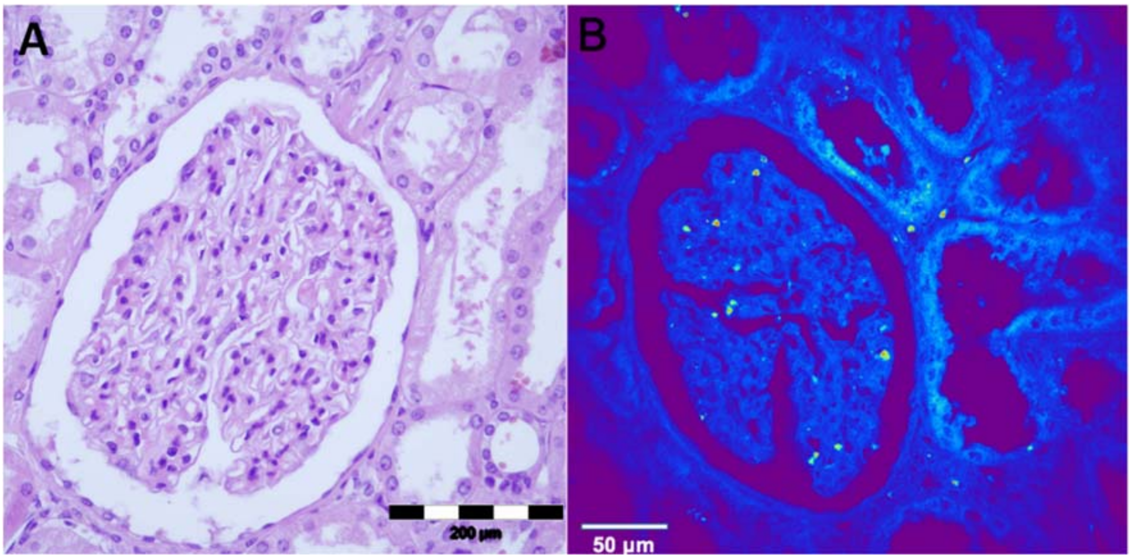

Figure 1. Healthy kidney tissue, (A) hematoxylin-eosin staining, light microscopy. Renal corpuscle is visible in the central part of the image, surrounded with proximal and distal tubules; (B) Unstained, TPEF. Renal corpuscle and tubules are comparable well recognized on unstained TPEF images.

The most common type of renal cell carcinoma is ccRCC. It shows characteristic morphological features observed using standard light microscopy. On H&E stained slides, ccRCC is characterized by round or oval cells with clear cytoplasm rich in glycogen and lipid droplets. Nuclei can show different degrees of differentiation. Tumor cells form solid nests or alveolar, acinar and cystic growing pattern surrounded by thin or thick fibrous septa (Figure 2A,D,G). These carcinomas typically contain a regular network of small blood vessels with a thin wall. Despite characteristic features of ccRCC, there are several diagnostic morphological pitfalls, arising mostly due to the occasional presence of eosinophilic cytoplasm and high nuclear grade features, as well as architectonic changes such as papillary growth patterns. However, these challenging cases could be successfully solved by IHC analyses. Among 43 cases of ccRCC, 13 cases were diagnosed as ccRCC with nuclear grades III and IV, while only two out of 13 cases contained prominent eosinophilic cytoplasm.

The majority of ccRCC samples obtained by the NLM technique showed a unique TPEF pattern. Nests of tumor cells and alveolar structures were distinguishable. Different sizes of nuclei were visible, predominantly eccentrically located, seen as bright areas due to higher TPEF signal. The cytoplasmic membrane is poorly distinguishable and tumor cells are surrounded with thin fibrous septa (Figure 2 B,E,H). Cells with homogeneous TPEF signal in the cytoplasm were identified (Figure 2E), presenting eosinophilic cells shown in Figure 2D. All NLM pictures were presented in original form (colored) and on gray scale for better comparison (Figure 2 C,F,I). Applying NLM technique we were able to diagnose 41 samples of ccRCC, while for 2 cases we made potential diagnosis of pRCC for one, and chRCC for another case. Moreover, one case of chRCC was misdiagnosed as ccRCC. Overall, the sensitivity of NLM technique for diagnosis of ccRCC was 95.3%, while the specificity was 98.1%.

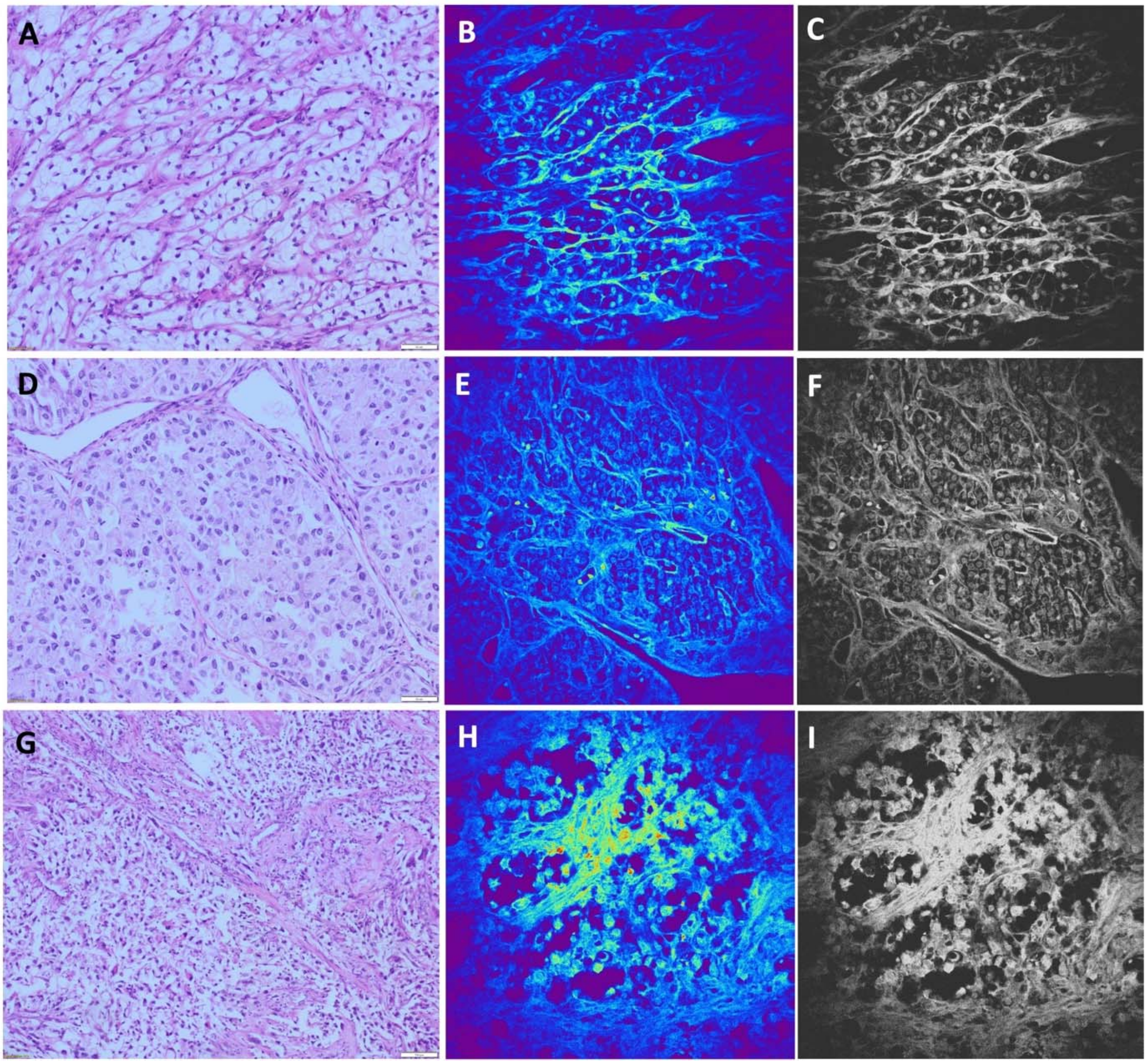

Figure 2. Clear cell renal carcinoma (A, D, G), hematoxylin-eosin staining, light microscopy. Tumor cells are forming alveolar nests surrounded by thick fibrous septa. Cells are round to oval, with clear cytoplasm. (B, E, H) Unstained, TPEF. Alveolar pattern of tumor cell growth, with surrounding thick fibrous septa, are visible. The tumor cell membrane is poorly distinguishable. TPEF signal from tumor cell cytoplasm is low in most cells. Nuclei of different size, predominantly eccentrically located are seen as variably bright areas. (C, F, I). Gray scale images of (B, E, H).

The papillary renal cell carcinomas (pRCC) on H&E stained slides are usually characterized by papillary or tubulopapillary architecture, having fibrovascular cores which may contain foamy macrophages, psammoma bodies and hemosiderin. These cells are cuboidal or cylindrical with basophilic or eosinophilic cytoplasm, having low or high nuclear grade depending on the type of the tumor. pRCC formerly classified as type I (Figure 3A), now is classified as low grade pRCC or classic variant, and pRCC formerly classified as type II, now is classified as high grade pRCC (Figure 3D,G). Usually, based on morphology and specific IHC findings diagnosis of pRCC could be easily made.

We were encouraged to investigate the ability of NLM to detect 15 pRCC cases among 96 renal tumor samples. Mostly, the distinctly papillary pattern, with a thin fibrovascular core lined with a layer of cuboidal/columnar cells, is seen on TPEF images. Nuclei were identified as regions with a weak signal and observed as dark areas (Figure 3B,E,H). In the core of papillae, collagen fibers and blood vessels can be recognized. (Figure 3B). Applying NLM technique we were able to diagnose 14 samples of pRCC, while for one case was diagnosed as solid variant of RO. Furthermore, we diagnosed one case as pRCC which belonged, according to morphological and IHC characteristics, to ccRCC with papillary architecture and eosinophilic cytoplasm. Finally, the sensitivity of NLM technique for diagnosis of pRCC was 93.3%, while the specificity was 98.7%.

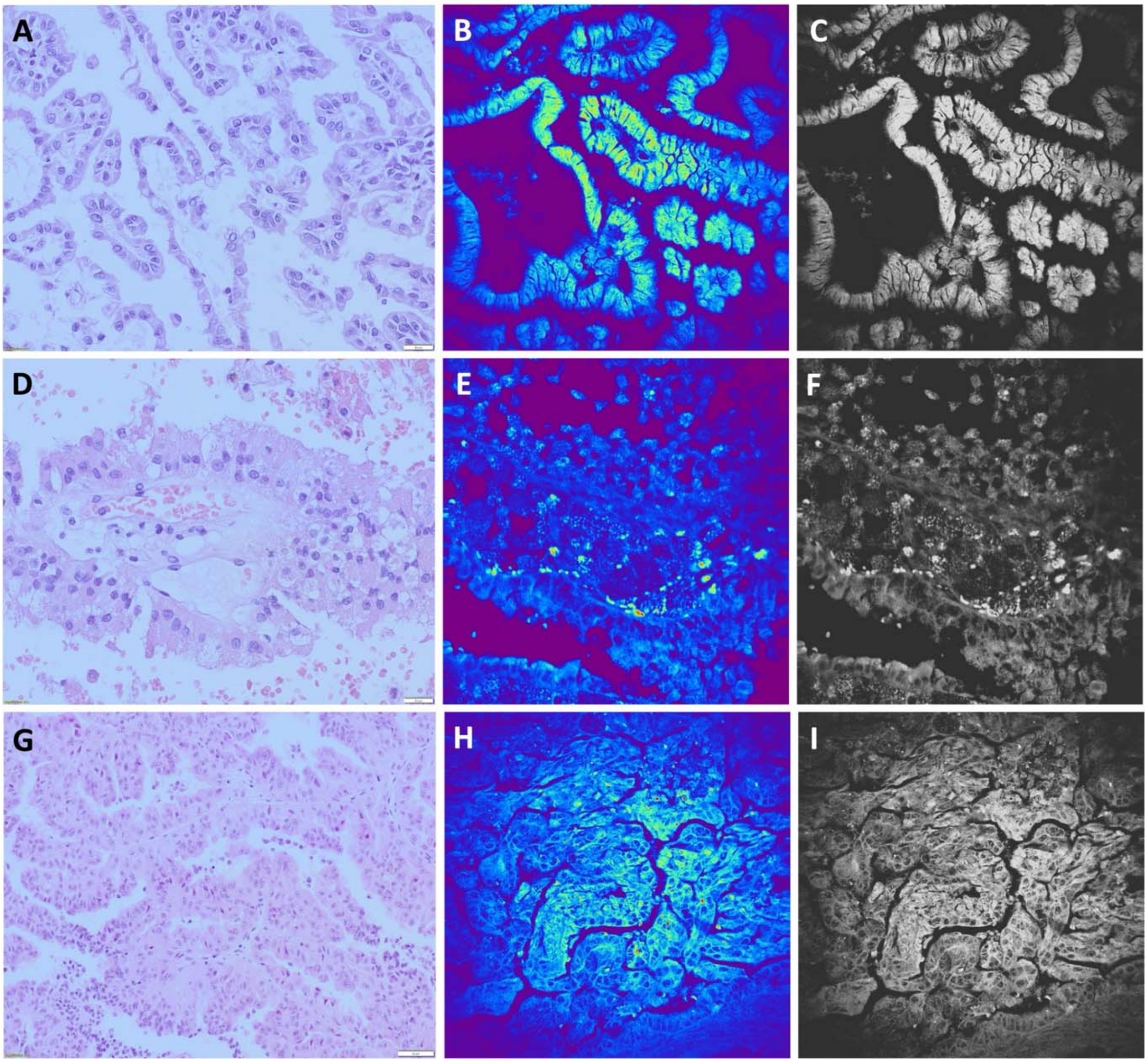

Figure 3. Papillary renal cell carcinoma (A, D, G) hematoxylin-eosin staining, light microscopy. Tumor cells are forming tubulopapillary structures with fibrovascular cores. Tumor cells are cuboidal to cylindrical with mildly pleomorphic oval to round nuclei. (B, E, H). Unstained, TPEF. The distinctly papillary pattern, with a thin fibrovascular core lined with a layer of cuboidal to columnar cells is seen. Nuclei could be identified as regions with weak TPEF signal. (C, F, I). Gray scale images of (B, E, H).

Chromophobe renal cell carcinoma (chRCC) is mostly characterized by cells arranged in solid nests surrounded by vascular septa. Cells can be large with pale cytoplasm or medium sized with granular eosinophilic cytoplasm. Nuclei are irregular with perinuclear haloes. Even binucleation can be seen. The cell membrane is prominent in both types of cells (Figure 4A,D,G).

In 19/20 analyzed images of chRCC obtained by NLM, we observed a prominent and thick cell membrane and a strong TPEF signal in the nuclei, which were recognized as centrally localized bright areas. A distinct perinuclear halo was mostly seen in medium sized cells. In the cytoplasm, on the periphery of the cells, higher signals can be detected in the form as granules (Figure 4B,E,H). One chRCC case composed exclusively of pale cells was misdiagnosed as ccRCC by NLM. Furthermore, based on nuclear and cytoplasmic features, despite of incomplete consensus based on membrane features, one case of ccRCC with eosinophilic cytoplasm was misdiagnosed as chRCC. According to

doi:10.20944/preprints202310.1864.v1

these analyses, the sensitivity of NLM technique for chRCC diagnosis was 95% with the specificity of 98.7%.

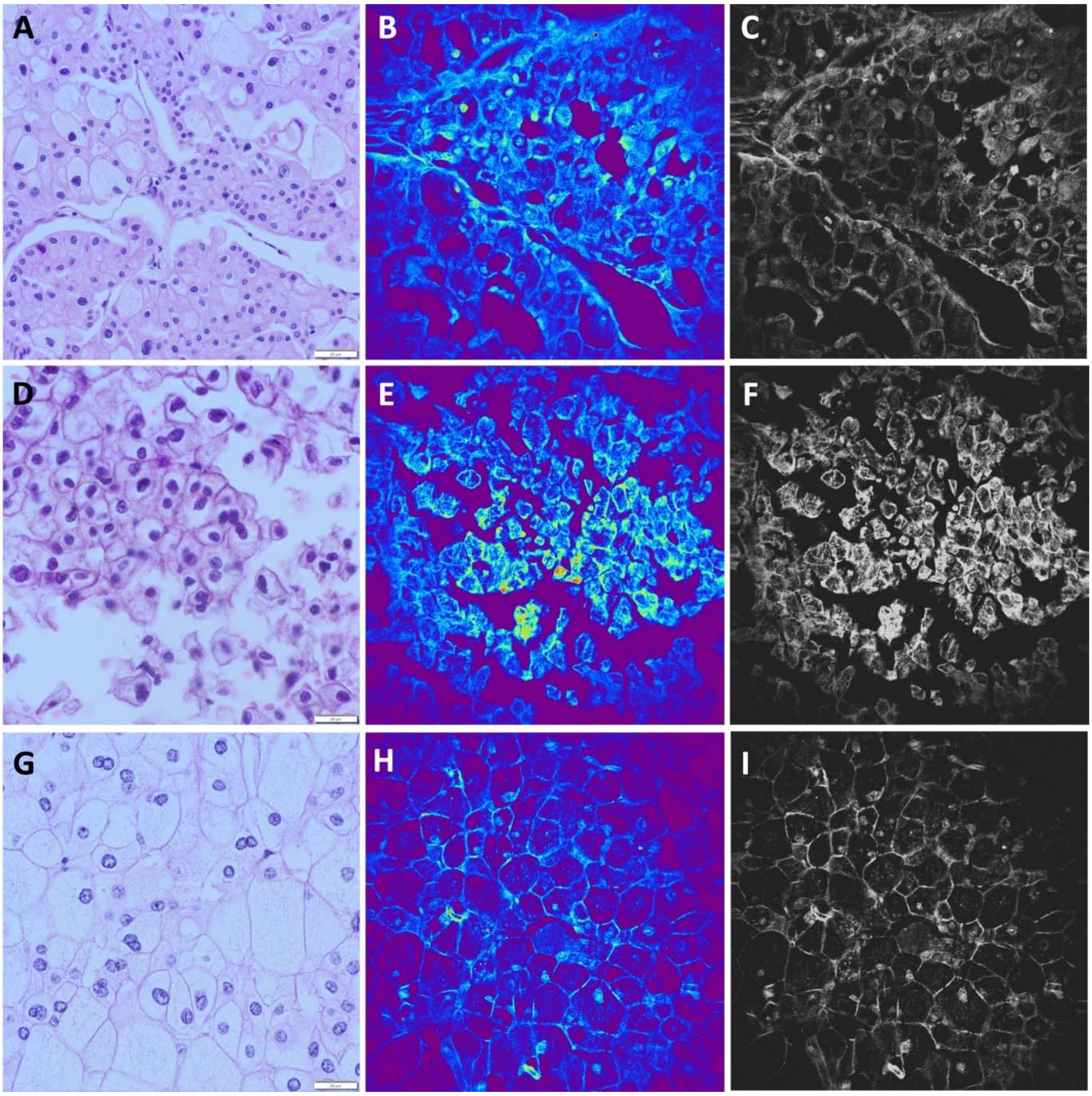

Figure 4. Chromophobe renal cell carcinoma (A, D, G), hematoxylin-eosin staining, light microscopy. Tumor cells are arranged in solid nests surrounded by thin vascular septa. Cells are large with eosinophilic granular cytoplasm. Nuclei are irregular with perinuclear haloes. (B, E, H) Chromophobe renal cell carcinoma, unstained, TPEF. Nested arrangement, "dusty" granular cytoplasm and perinuclear halos are clearly discernable using NLM. (C, F, I). Gray scale images of (B, E, H).

In contrast to the TPEF signal observed in ccRCC, pRCC, and chRCC, the TPEF signal detected in RO exhibits considerably greater intensity (Figure 5B). This heightened intensity can be attributed to the presence of granular cytoplasm abundant in mitochondria. The cellular morphology is characterized by cuboidal cells, with nuclei appearing as dark regions due to a diminished TPEF signal. These nuclei are arranged in a microcystic pattern and less frequently in solid nests. Consequently, distinct NLM features consistently identified all RO samples, resulting in a method sensitivity of 100%. However, a marginal reduction in specificity to 98.7% was noted, primarily due to a single false positive case that was initially misidentified as RO but was later confirmed to be a solid variant of pRCC.

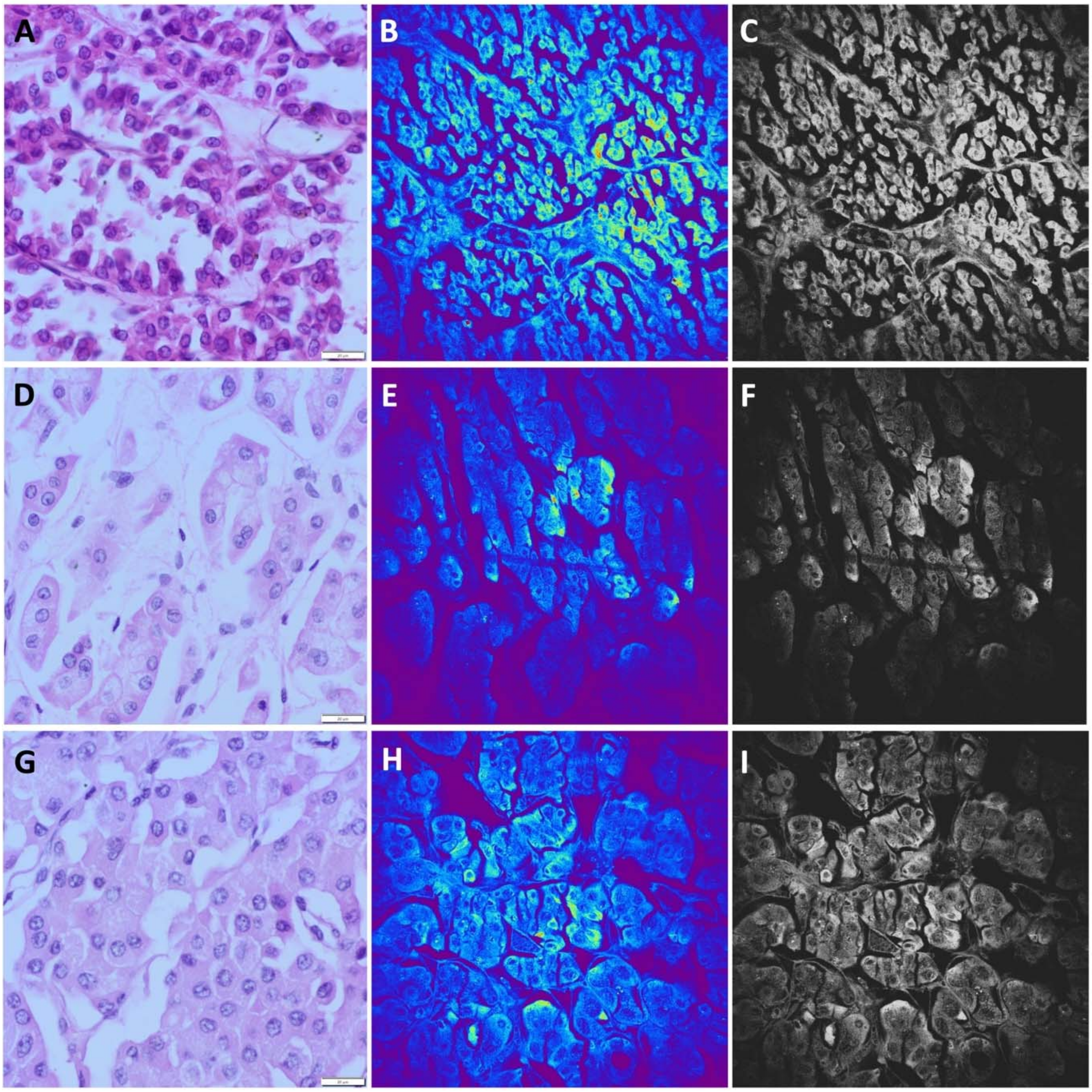

Figure 5. Renal cell oncocytoma (A, D, G) hematoxylin-eosin staining, light microscopy. Cytoplasm is bright eosinophilic, granular. (B, E, H) Renal cell oncocytoma, unstained, TPEF. Cells are mainly uniform with highly granular cytoplasm and are characterized by strong TPEF signal and pale round nuclei, due to weak TPEF signal. The scale bars in figures A and B are 200 μm and 50 μm, respectively. (C, F, I). Gray scale images of (B, E, H).

Overall, among 96 analyzed kidney tumors by NLM technique we were able to precisely diagnose the 92 of them., leading to the diagnostic accuracy of 95,8%.

Subsequently, we employed the SHG technique to visualize the collagen matrix, serving as a highly dynamic support structure for tumor cells. The composition and arrangement of collagen exhibit notable variability across distinct renal tumor types. Additionally, within patients presenting the same tumor type, discernible variations primarily concerning collagen quantity are prevalent. In the case of ccRCC, the SHG signal is robust, indicative of a well-organized collagen network surrounding the alveolar tumor cell clusters. Similarly, SHG signal intensity is significant in pRCC samples. Here, we observed slender collagen strands lining the papillary structures and parallel collagen fibers filling the core of the papillae. Conversely, both in RO and chRCC, the SHG signal is comparatively weaker than in ccRCC and pRCC. Nonetheless, it still allows for the visualization of delicate collagen strands that separate groups of tumor cells. In all tumor types, a prominent SHG signal emanating from the intricate network of blood vessels is evident, most prominently in ccRCC and pRCC.

The presence of a discernible capsule surrounding the tumors was readily evident in the SHG images. The SHG signal originating from the capsule exhibited distinct characteristics, appearing wavy, thick, dense, predominantly parallel, and well-organized in structure, primarily composed of collagen. Additionally, intracapsular blood vessels were observed. Figure 6 presents a visual representation of these findings.

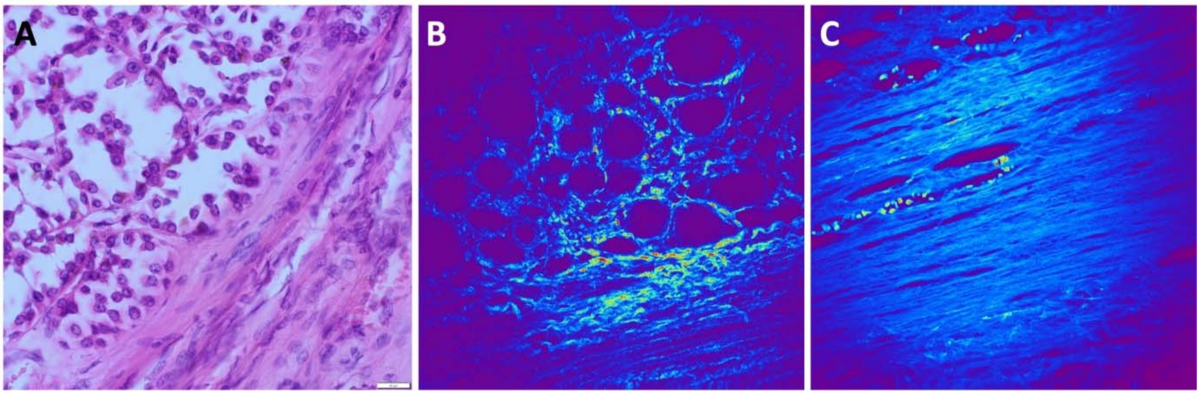

Figure 6. SHG imaging of the collagen fibers. (A) H&E slide of RO with tumor capsule. (B), SHG image unstained, collagen forms a network around alveolar nests of tumor cells. (C) In the capsule around ccRCC, collagen fibers are thick, mostly parallel and orderly organized. The elongated holes lined with collagen fibers represent intracapsular blood vessels. The scale bars in all figures are 50 µm.

4. Discussion

In this study, we utilized nonlinear (multiphoton) microscopy, including two-photon excitation fluorescence (TPEF) and second harmonic generation (SHG) techniques, for the evaluation of renal cell tumors, specifically focusing on clear cell renal cell carcinoma (ccRCC), papillary renal cell carcinoma (pRCC), chromophobe renal cell carcinoma (chRCC), and renal oncocytoma (RO).

The use of nonlinear microscopy, particularly multiphoton microscopy, has gained traction in recent years for studying various types of tumors, including urothelial, breast, pancreatic, colorectal carcinoma, and others (21-25). This technique offers advantages such as label-free imaging, deeper tissue penetration, reduced phototoxicity, and enhanced spatial resolution (1-5). For kidney tumors, the morphological overlap observed in traditional H&E-stained slides, especially between chRCC and RO, makes differentiation challenging (26). Therefore, employing advanced imaging techniques like nonlinear microscopy is crucial for accurate tumor subtyping and diagnosis.

Jain et al. pioneered the application of nonlinear microscopy techniques for kidney tumor evaluation, demonstrating the potential of NLM in subcategorizing tumors based on nuclear-cytoplasmic ratio (N/C ratio) and nuclear pleomorphisms, rather than the intranuclear characteristics, because the NLM is not able to give intranuclear details (27). Based on the tumor tissue architecture, they classified cases into those with non-papillary and papillary morphology. Moreover, non-papillary tumors, based on the cytoplasmic features, were classified as clear cell renal cell carcinomas (ccRCCs) and chromophobe RCCs (chRCCs), considering distinct identifiable features. Applying this method, Jain et al. reached the diagnostic accuracy of 95% in kidney tumor subtyping. Although, this cohort included in total 40 tumor samples and did not consider benign tumors, the diagnostic accuracy was comparable with our results (95.8%), that were obtained by the analyses of 96 kidney tumors, including benign RO. Moreover, our study builds on this foundation by exploring the detailed NLM characteristics of different renal cell tumors, focusing on features like cytoplasmic boundary, collagen content, and cell membrane characteristics. Beside the calculation of overall diagnostic NLM accuracy, we specifically defined the specificity and sensitivity of this method in diagnosis of each kidney tumor subtype, that was high in general. Considering the challenge to differentiate benign tumors from those with malignant biological behavior, that require contrasting paths of therapeutic management (26), using AF and SHG, as NLM methods, Jain et al. differentiated oncocytomas (typical and atypical) and chRCC, as the tumors are often considered to be part of the same morphological spectrum of diseases (26). Introducing the morphometric analysis of NLM imaging, they revealed the absolute diagnostic accuracy for oncocytomas (100%) and the high accuracy for chRCC (83.3%). In their study, NLM of these tumors showed autofluorescent intracytoplasmic granules, with distinct sizes, shapes, distribution and different wavelengths of autofluorescence. The eosinophilic variant of chRCC (one case) also had a distinct autofluorescent nucleus and perinuclear halo (26). Moreover, our diagnostic accuracy for RO was 100%, and 95% for chRCC. However, we found that other tumors different from chRCC could be misdiagnosed as RO, based on NLM features.

Utilizing NLM techniques, Galli and Sablinskas elucidated that typical kidney tissue exhibited a distinct structural organization, characterized by the presence of tubules and an abundant vascular network. The blood vessels demonstrated a stratified composition consisting of collagen and elastin, setting them apart from the tubular structures. Notably, they differentiated RO from healthy renal parenchyma, the latter displaying a significantly different morphology devoid of the characteristic tubular arrangements. Upon closer inspection, a discernible demarcation between normal and RO tissues became evident, marked by the prevalence of collagen-rich structures. RO tissues showcased aggregates of epithelial cells interspersed with delicate stromal elements, a characteristic feature of these tumors. Collagen structures within ROs exhibited a diminished SHG signal intensity compared to normal tissues; however, they remained distinctly identifiable. These findings underscored the potential of NLM in delineating tumor boundaries and imparting valuable insights into the distinctive morphological characteristics that distinguish various subtypes of renal cell tumors. Notably, NLM outperforms conventional H&E staining in terms of the wealth of information it furnishes. While H&E staining primarily accentuates cell nuclei and nonspecific tissue proteins, multimodal NLM unveils tissue morphology based on its compositional attributes. It achieves visualization of intracellular and extracellular lipids through coherent anti-Stokes Raman scattering (CARS) and extracellular matrix proteins like collagen and elastin via second harmonic generation (SHG) and two-photon excitation fluorescence (TPEF) (28).

Besides investigation into kidney tumors, NLM has also been introduced in the investigation of non-neoplastic renal diseases. Huang and Liu observed in their study that NLM, encompassing techniques TPEF and SHG imaging, efficiently captured tissue and cell morphology in kidney biopsy specimens without staining or labeling. This comprehensive visualization encompassed glomeruli, renal tubules, interstitial areas, and blood vessels. Additionally, both NLM and Masson trichrome staining facilitated the identification of normal glomeruli and glomerulosclerosis, with NLM's TPEF signals appearing more pronounced in sclerotic glomeruli, possibly due to increased autofluorescence. Furthermore, NLM, particularly through SHG imaging, effectively revealed collagen deposition in the tubular interstitial area, a hallmark of interstitial fibrosis, thus enabling the assessment of its extent. Finally, the combination of TPEF and SHG in NLM facilitated the recognition of tubular atrophy and other tubular interstitial changes, mirroring observations in Masson trichrome stained images (29).

Considering our previous finding with regard to the utility of mitochondria staining in the differentiation of renal cell tumor types (30), here we carried out NLM technique in order to compare the findings with literature data, as well as to explore possible overlapping of NLM data with the previously found differences in mitochondria distribution.

In the kidney, SHG is produced by collagen and the extent of collagen formation can be quantified based on the separation of SHG and autofluorescence in the phasor plot (1-7SHG) (16). Our NLM techniques revealed ccRCC was identified by poorly distinguishable cytoplasmic boundary and tumor cells surrounded by thin fibrous septa that contain the collagen fibers, as seen in SHG images. The main tissue components responsible for SHG generation are myosin and collagen fibers, particularly collagen 1, as these fibers are non-centrosymmetric in structure (31,32). Moreover, we found that in pRCC the fibrovascular core could be easily visualized with SHG, while with TPEF we could observe cells lining the fibrovascular core, arranged in a single layer or multiple pseudolayers and psammoma bodies. Also, the tumorous capsule that divides tumor and healthy tissue is clearly observed, implicating that the SHG technique could be utilized for detection of surgical margins. The nuclei in both ccRCC and pRCC are characterized by their brightness, primarily due to a relatively weak signal. In ccRCC, the cytoplasm exhibits either weak autofluorescence or an absence of it, attributed to the presence of lipids, glycogen, and a reduced number of mitochondria. Conversely, in the case of pRCC, there is stronger autofluorescence, particularly at the apical region, accompanied by a mild signal surrounding the nuclei. In TPEF images, chRCC is characterized by a unique features, such as a prominent cell membrane and a perinuclear halo, effectively distinguishing it from both ccRCC and pRCC. More pronounced TPEF signal, in the periphery of chRCC cells, becomes evident specifically at higher magnification, and is visualized in the form of a multitude of small granules. In the case of both ccRCC and pRCC, nuclei are centrally located and appear as bright regions. While there may be morphological similarities between chRCC and RO on H&E slides, the TPEF signal in RO nuclei presents as a dark area, in contrast to the chRCC pattern. Another distinction between chRCC and RO lies in the TPEF signal within the cytoplasm, which is more pronounced in the case of RO. When explored at higher magnification, the signal observed in RO consists of numerous granules that can vary in size, in contrast to the chRCC scenario where the granules are predominantly small and uniform.

In general, most of our results align with the existing literature. Nevertheless, while previous studies have extensively described the nuclear and cytoplasmic attributes of tumor cells, there has been limited exploration of cell membrane characteristics. Our research has revealed several distinctive features. In ccRCC samples, cell membranes are notably indistinct and relatively slender in comparison to other tumor types. In contrast, chRCC displays the most pronounced and thick membranes, a feature not observed in other morphologically similar types of RCC.

NLM has been a subject of investigation in various types of tumors. In their study, Cahill and Fujimoto engaged genitourinary pathologists to assess 70 NLM images alongside corresponding paraffin H&E images of prostate specimens. They observed distinctions between NLM and H&E images, particularly in terms of cytoplasmic color and stromal density. NLM allowed for the visualization of various components, such as benign, atrophic, and hyperplastic glands, stromal features, ejaculatory ducts, vasculature, inflammatory changes, as well as the identification of different adenocarcinoma variants and Gleason patterns. Furthermore, NLM facilitated the assessment of critical factors like perineural invasion and extraprostatic extension. An important disparity between NLM and H&E images was the color representation, as NLM images utilize fluorescence signals, resulting in color variations compared to traditional H&E staining. Features reliant on color, such as pale pink cytoplasm or the appearance of red blood cells, were less consistent and evident in NLM images, including the cytoplasm of foamy variant adenocarcinoma (33).

Beletkaya and Dashtobozorog, in their research, investigated the intensity distribution of Second Harmonic Generation (SHG) and Two-Photon Excited Fluorescence (TPEF) signals within breast tissue samples. They noted variations in intensity distribution, especially in the TPF signal, which exhibited a distinct peak in regions corresponding to cancerous cells with higher signal intensity. Changes in collagen quantity and organization were also observed in areas of invasive ductal carcinoma and tumor progression, compared to unaltered breast tissue. Additionally, polarimetric SHG proved useful for molecular classification of breast carcinomas, revealing ultrastructural disorganization in different molecular subtypes of breast carcinoma. Furthermore, specific collagen fiber organization patterns were identified in unique tumor types such as tubular carcinoma, invasive lobular carcinoma, medullary, mucinous, and papillary carcinomas. Organized collagen fibers were found in ductal carcinoma in situ, and the application of therapeutic agents induced alterations in collagen parameters. These changes may provide insights into the mechanisms of tumor progression and response to therapy. Differences in collagen deposition allowed for the distinction between fibroadenoma and phyllodes tumors with high sensitivity and specificity (34-44).

Galli and Siciliano conducted an investigation into colorectal liver metastases and hepatic tissue using Coherent Anti-Stokes Raman Scattering (CARS), TPEF, and SHG. Their analysis involved more than 40,000 NLM images, enabling the differentiation of normal liver from metastatic tissue and the delineation of tumor borders in cryosections and formalin-fixed bulk tissue. Notably, NLM offers several advantages, including the elimination of the need for freezing and cryotoming, rendering it a faster and non-destructive alternative to frozen section analysis. NLM's capability to provide depth-resolved imaging up to 100 μm beneath the tissue surface proved valuable in gaining insights into architectural morphology at various tissue depths (45).

5. Conclusions

In conclusion, our study underscores the potential of nonlinear microscopy, particularly NLM, in enhancing the diagnostic accuracy of renal cell tumors. By exploring unique characteristics of different renal cell tumor subtypes, such as cytoplasmic boundary, collagen content, and cell membrane features, NLM can aid in accurate subtyping and diagnosis. Nonlinear microscopy offers a promising future in the field of pathology, potentially revolutionizing the way we diagnose and subtype various cancers. Further research should focus on standardizing these techniques, exploring their potential for in vivo imaging, and integrating artificial intelligence algorithms for automated analysis, ultimately enhancing diagnostic accuracy and clinical outcomes for patients with renal cell tumors.

Author Contributions: conceptualization- GN and MZ.; methodology- G.N.; formal analysis, L.M, G.N, M.Z.; investigation, G.N., A.M., S.D., S.N, M.R; data curation, G.N., M.Z., A.M., S.D., S.N, M.R; writing—original draft preparation, G.N., M.Z., A.M., S.D., S.N, M.R; writing—review and editing, L.M., S.R.S.; visualization, L.M.; supervision, L.N.; funding acquisition, S.N., M.R., L.M. All authors have read and agreed to the published version of the manuscript.

Funding: This research was funded by the Ministry of Education, Science, and Technological Development of the Republic of Serbia (project Nos. III41006).

Institutional Review Board Statement: The study was conducted in accordance with the Declaration of Helsinki and approved by the Professional Board of the Clinic for Urology, Clinical Centre of Serbia (protocol code 0152, 4 March 2020) for studies involving human tissues.

Informed Consent Statement: Patient consent was waived because according to the policy of our Ethics Committee it is not required for retrospective studies, especially considering that the material used in this study was collected from the archive after diagnostic work was completed.

Data Availability Statement: All data are provided within the manuscript

Acknowledgments: S.N. and M.R. acknowledge funding provided by the Institute of Physics Belgrade, through the grant by the Ministry of Science, Technological Development, and Innovation of the Republic of Serbia.

Conflicts of Interest: The authors declare no conflict of interest. The funders had no role in the design of the study, in the collection, analyses or interpretation of data, in the writing of the manuscript or in the decision to publish the results.

References

1. Zipfel WR, Williams RM, Webb WW. Nonlinear magic: multiphoton microscopy in the biosciences. *Nat Biotechnol* **2003**; *21*, 1369-77.
2. Denk W, Strickler JH, Webb WW. Two-photon laser scanning fluorescence microscopy. *Science.* **1990,** *6*; 73-6.
3. Xu C, Zipfel W, Shear JB, Williams RM, Webb WW. Multiphoton fluorescence excitation: new spectral windows for biological nonlinear microscopy. *Proc Natl Acad Sci U S A.* **1996**, *1;93(20*), 10763-8.
4. Zipfel WR, Williams RM, Christie R, et al. Live tissue intrinsic emission microscopy using multiphoton-excited native fluorescence and second harmonic generation. *Proc Natl Acad Sci U S A* **2003**; *100*, 7075-80.
5. Mertz J. Optical sectioning microscopy with planar or structured illumination. *Nat Methods* **2011**; *8*, 811-9.
6. Mertz J. Nonlinear microscopy: new techniques and applications. *Curr Opin Neurobiol*. **2004** *14(5)*, 610-6.
7. Ranawat, H., Pal, S. & Mazumder, N. Recent trends in two-photon auto-fluorescence lifetime imaging (2P-FLIM) and its biomedical applications. *Biomed. Eng. Lett.* **2019,** *9*, 293–310.

8. Parodi V, Jacchetti E, Osellame R, Cerullo G, Polli D, Raimondi MT. Nonlinear Optical Microscopy: From Fundamentals to Applications in Live Bioimaging. *Front Bioeng Biotechnol*. **2020**, *9*, 8:585363.
9. Gopal AA, Kazarine A, Dubach JM, Wiseman PW. Recent advances in nonlinear microscopy: Deep insights and polarized revelations. *Int J Biochem Cell Biol*. **2021** *130*, 105896.
10. Horton NG, Wang K, Kobat D, Clark CG, Wise FW, Schaffer CB, Xu C. *In vivo* three-photon microscopy of subcortical structures within an intact mouse brain. *Nat Photonics*. **2013,** *1*;7(3), 205–9.
11. Ouzounov DG, Wang T, Wang M, Feng DD, Horton NG, Cruz-Hernández JC, Cheng YT, Reimer J, Tolias AS, Nishimura N, Xu C. In vivo three-photon imaging of activity of GCaMP6-labeled neurons deep in intact mouse brain. *Nat Methods*. **2017** *14(4)*, 388-390.
12. König, T. T., Goedeke, J., and Muensterer, O. J. Multiphoton microscopy in surgical oncology- a systematic review and guide for clinical translatability. *Surg. Oncol.* **2019**, *31*, 119–131.
13. Sanderson, M. J., Smith, I., Parker, I., and Bootman, M. D. Flourescence microscopy. *Cold Spring Harb. Protoc.* **2016**, 2014:36.
14. Helmchen, F., and Denk, W. Deep tissue two-photon microscopy. *Nat. Methods*, **2005**, *2*, 932–940.
15. Hoover, E. E., and Squier, J. A. Advances in multiphoton microscopy technology. *Nat. Photonics*, **2013**, *7*, 93–101.
16. Ranjit S, Lanzanò L, Libby AE, Gratton E, Levi M. Advances in fluorescence microscopy techniques to study kidney function. *Nat Rev Nephrol*. **2021**, *17(2)*, 128-144.
17. Hall AM, Schuh CD, Haenni D. New frontiers in intravital microscopy of the kidney. Curr Opin Nephrol Hypertens. **2017,** *26(3*), 172-178.
18. Sandoval RM, Molitoris BA. Intravital multiphoton microscopy as a tool for studying renal physiology and pathophysiology. *Methods.* **2017**, *1;128*, 20-32.
19. Molitoris BA, Sandoval RM, Wagner MC. Intravital Multiphoton Microscopy as a Tool for Studying Renal Physiology, Pathophysiology and Therapeutics. *Front Physiol*. **2022,** 24;13:827280.
20. Treacy PJ, Khosla A, Kyprianou N, Falagario UG, Tsavaras N, Wiklund P, Tewari AK, Durand M. Value of multiphoton microscopy in uro-oncology: a narrative review. *Transl Androl Urol*. **2023** *31;12(3)*, 508-518.
21. Mukherjee S, Wysock JS, Ng CK, Akhtar M, Perner S, Lee M, Rubin MA, Maxfield FR, Webb WW, Scherr DS. Human bladder cancer diagnosis using multiphoton microscopy. *Proc. SPIE 7161, Photonic Therapeutics and Diagnostics V*, **2009,** 716117.
22. Wu X, Chen G, Lu J, Zhu W, Qiu J, Chen J, Xie S, Zhuo S, Yan J. Label-free detection of breast masses using multiphoton microscopy. *PLoS One*. **2013**, *6;8(6)*, e65933.
23. Yan J, Zhuo S, Chen G, Milsom JW, Zhang H, Lu J, Zhu W, Xie S, Chen J, Ying M. Real-time optical diagnosis for surgical margin in low rectal cancer using multiphoton microscopy. *Surg Endosc*. **2014,** *28(1)*, 36-41.
24. Hu W, Zhao G, Wang C, Zhang J, Fu L. Nonlinear optical microscopy for histology of fresh normal and cancerous pancreatic tissues. *PLoS One*. **2012**, *7(5*), 37962.
25. Lopez DR, Sgroi D, Krishnamourthy S, Tearney G. Is Real-Time Microscopy on the Horizon? A Brief Review of the Potential Future Directions in Clinical Breast Tumor Microscopy Implementation. *Virchows Arch*. **2022,** *480*, 211-227.
26. Jain M, Robinson BD, Wu B, Khani F, Mukherjee S. Exploring Multiphoton Microscopy as a Novel Tool to Differentiate Chromophobe Renal Cell Carcinoma From Oncocytoma in Fixed Tissue Sections. *Arch Pathol Lab Med*. **2018**, *142*, 383-390.
27. Jain M, Robinson BD, Aggarwal A, et al. Multiphoton microscopy for rapid histopathological evaluation of kidney tumours. *BJU Int*, **2016**; *118*, 118-26.
28. Galli R, Sablinskas V, Dasevicius D, Laurinavicius A, Jankevicius F, Koch E, Steiner G. Non-linear optical microscopy of kidney tumours. *J Biophotonics.* **2014,** *7*, 23-7.
29. Huang HW, Liu D, Hu JM, Xu SY, Zhuo SM, Liu YG, Zhao M. Application of Nonlinear Optical Microscopic Imaging Technology for Quality Assessment of Donor Kidneys. *Transplant Proc*. **2018,** *50(10),* 3128-3134.
30. Nikolic, G.; Zivotic, M.; Cirovic, S.; Despotovic, S.; Dundjerovic, D.; Radojevic Skodric, S. The Utility of Mitochondrial Detection Methods Applied as an Additional Tool for the Differentiation of Renal Cell Tumors. *Diagnostics,* **2023**, *13*, 2319.
31. Chen, X., Nadiarynkh, O., Plotnikov, S. *et al.* Second harmonic generation microscopy for quantitative analysis of collagen fibrillar structure. *Nat Protoc*, **2012**, 7, 654–669.
32. Campagnola P. Second harmonic generation imaging microscopy: applications to diseases diagnostics. *Anal Chem*. **2011,** *1;83(9*), 3224-31.

33. Cahill LC, Fujimoto JG, Giacomelli MG, Yoshitake T, Wu Y, Lin DI, Ye H, Carrasco-Zevallos OM, Wagner AA, Rosen S. Comparing histologic evaluation of prostate tissue using nonlinear microscopy and paraffin H&E: a pilot study. *Mod Pathol*. **2019** *32(8),* 1158-1167.
34. Beletkaia E, Dashtbozorg B, Jansen RG, Ruers TJM, Offerhaus HL. Nonlinear multispectral imaging for tumor delineation. *J Biomed Opt*. **2020**, *25(9)*, 096001.
35. Natal RA, Vassallo J, Paiva GR, et al. Collagen analysis by second-harmonic generation microscopy predicts outcome of luminal breast cancer. *Tumor Biology*. **2018**, *40(4).*
36. Brabrand A, Kariuki II, Engstrøm MJ, Haugen OA, Dyrnes LA, Åsvold BO, Lilledahl MB, Bofin AM. Alterations in collagen fibre patterns in breast cancer. A premise for tumour invasiveness? *APMIS*. **2015,** *123(1)*, 1-8.
37. Lopez DR, Sgroi D, Krishnamourthy S, Tearney G. Is Real-Time Microscopy on the Horizon? A Brief Review of the Potential Future Directions in Clinical Breast Tumor Microscopy Implementation. *Virchows Arch*. **2022**, *480(1)*, 211-227.
38. Golaraei A, Kontenis L, Cisek R, Tokarz D, Done SJ, Wilson BC, Barzda V. Changes of collagen ultrastructure in breast cancer tissue determined by second-harmonic generation double Stokes-Mueller polarimetric microscopy. *Biomed Opt Express*. **2016,** *15;7(10),* 4054-4068.
39. Adur J, Pelegati VB, de Thomaz AA, D'Souza-Li L, Assunção Mdo C, Bottcher-Luiz F, Andrade LA, Cesar CL. Quantitative changes in human epithelial cancers and osteogenesis imperfecta disease detected using nonlinear multicontrast microscopy. *J Biomed Opt.* **2012,** *17(8)*, 081407-1.
40. Natal, R.d., Paiva, G.R., Pelegati, V.B. *et al.* Exploring Collagen Parameters in Pure Special Types of Invasive Breast Cancer. *Sci Rep*, **2019**, 9, 7715.
41. Conklin MW, Gangnon RE, Sprague BL, Van Gemert L, Hampton JM, Eliceiri KW, Bredfeldt JS, Liu Y, Surachaicharn N, Newcomb PA, Friedl A, Keely PJ, Trentham-Dietz A. Collagen Alignment as a Predictor of Recurrence after Ductal Carcinoma *In Situ*. *Cancer Epidemiol Biomarkers Prev*. **2018,** *27(2)*, 138-145.
42. Walsh AJ, Cook RS, Lee JH, Arteaga CL, Skala MC. Collagen density and alignment in responsive and resistant trastuzumab-treated breast cancer xenografts. *J Biomed Opt*. **2015,** *20*(*2*), 26004.
43. Bredfeldt JS, Liu Y, Pehlke CA, Conklin MW, Szulczewski JM, Inman DR, Keely PJ, Nowak RD, Mackie TR, Eliceiri KW. Computational segmentation of collagen fibers from second-harmonic generation images of breast cancer. *J Biomed Opt.* **2014**, *19(1)*, 16007.
44. Nie YT, Wu Y, Fu FM, Lian YE, Zhuo SM, Wang C, Chen JX. Differentiating the two main histologic categories of fibroadenoma tissue from normal breast tissue by using multiphoton microscopy. *J Microsc*. **2015,** *258(1)*, 79-85.
45. Galli, R., Siciliano, T., Aust, D. *et al.* Label-free multiphoton microscopy enables histopathological assessment of colorectal liver metastases and supports automated classification of neoplastic tissue. *Sci Rep*, **2023,** *13*, 4274.